LAWRENCE
LIVERMORE
NATIONAL
LABORATORY

LLNL-JRNL-635120

Partitioning of Seismo-Acoustic Energy and Estimation of Yield and Height-of-Burst/Depth-of-Burial for Near-Surface Explosions

S. R. Ford, A. J. Rodgers, H. Xu, D. C. Templeton, P. E. Harben, W. Foxall, R. E. Reinke

April 12, 2013

Bulletin of the Seismological Society of America

Disclaimer

Partitioning of Seismo-Acoustic Energy and Estimation of Yield and Height-of-Burst/Depth-of-Burial for Near-Surface Explosions

Sean R. Ford[1], Arthur J. Rodgers[1], Heming Xu[1,2], Dennise C. Templeton[1], Philip Harben[1], William Foxall[1,3] and Robert E. Reinke[4]

[1] *Atmospheric, Earth and Energy Division, Lawrence Livermore National Laboratory, Livermore, CA 94551*

[2] now at *High Performance Geocomputing Lab, San Diego Supercomputer Center, La Jolla CA 92093*

[3] now at *Lawrence Berkeley National Laboratory, Berkeley, CA*

[4] *Defense Threat Reduction Agency, Kirtland Air Force Base, Albuquerque, NM 87117*

Manuscript prepared for the *Bulletin of the Seismological Society of America*

April 24, 2013

Abstract

Explosions near the Earth's surface excite both seismic ground motions and atmospheric overpressure. The energy transferred to the ground and atmosphere from a near-surface explosion depends on yield (W) as well as the height-of-burst/depth-of-burial (HOB/DOB) for above/below ground emplacements. We report analyses of seismic and overpressure motions from the Humble Redwood series of low-yield, near-surface chemical explosions with the aim of developing quantitative models of energy partitioning and a methodology to estimate W and HOB/DOB. The effects of yield, HOB and range on amplitudes can be cast into separable effects of amplitude as functions of scaled range and scaled HOB. We find that displacement of the initial P-wave and the integral of the positive overpressure (impulse) are diagnostic of W and HOB with minimal scatter. An empirical model describing the dependence of seismic and air-blast measurements on W, HOB/DOB and range is determined and model parameters are found by regression. We find seismic amplitudes for explosions of a given yield emplaced at or above the surface are reduced by a factor of 3 relative to fully contained explosions below ground. Air-blast overpressure is reduced more dramatically, with impulse reduced by a factor of 100 for deeply buried explosions relative to surface blasts. Our signal models are used to invert seismic and overpressure measurements for W and HOB and we find good agreement (W errors < 30%, HOB within meters) with ground truth values for four non-circular validation tests. While there is a trade-off between W and HOB for a single seismic or overpressure measurement, the use of both measurement types allows us to largely break this trade-off and better constrain W and HOB.

Introduction

The Earth's surface represents a drastic change in material properties between the solid earth and the fluid atmosphere. Explosions near this interface excite overpressure motions in the atmosphere and seismic motions in the solid Earth. These phenomena have received interest recently and are together referred to as seismo-acoustics (Arrowsmith et al., 2010; Bonner et al., 2013). This study aims to develop a quantitative understanding of seismo-acoustic energy partitioning with the ultimate goal of developing methodologies to estimate the yield (W) and emplacement of near-surface explosions from measurements of the seismo-acoustic wavefield. The emplacement refers to height-of-burst (HOB) for above-ground or depth-of-burial (DOB) for below-ground explosions (henceforth, DOB>0 and HOB<0 for buried explosions). In this study we focus on near-surface explosions meaning those with an absolute scaled HOB of approximately 2 $m/kg^{1/3}$ where the height (or depth for DOB) is scaled by the cube-root of the yield. Normal DOB for containment of historical NTS nuclear explosions is ~1.2 $m/kg^{1/3}$ (120 $m/kt^{1/3}$ (U. S. Office of Technology Assessment, 1989). We are interested in data recorded at local distances (<10 km) where the seismic motions are elastic but the cumulative effects of propagation (e.g. geometric spreading, scattering, attenuation) are minimized compared to regional or teleseismic distances. At these local ranges the overpressure mostly behaves as an air-blast, or shock-wave obeying hydrodynamic scaling. At longer range, atmospheric overpressure transitions from air-blast to acoustic motions and then to infrasound. Long-range infrasound typically interacts with altitude- and range-dependent atmospheric properties and this strongly impacts the timing, amplitude and waveform of the recorded overpressure signals.

However, local distance air-blast experiences less atmospheric variability. We define near-source scaled distance (r_s) as less than approximately 1000 m/kg$^{1/3}$ or 10,000 m/kt$^{1/3}$.

There is a rich literature on seismic motions from deeply buried explosions motivated by nuclear test hazard and monitoring. A few particular studies are relevant to this study. Adams et al. (1961) and Murphy and Lahoud (1969) reported empirical scaling relations for far-field seismic motions (displacement, velocity and acceleration) versus range. Many studies have found different behavior for explosions from different emplacement material strength (e.g., Perret and Bass, 1975) or recording site lithology (e.g., Murphy and Lahoud, 1969). Denny and Johnson (1991) provide a rich description of historical efforts.

The literature on seismic motions from surface explosion is smaller, however there are several important studies that inform our investigations. Murphy (1981) and Murphy and Shah (1988) investigated the coupling of explosion blast-waves into seismic motions and found that the dominant source of displacement is due to low-frequency surface waves. Kitov et al. (1997) described seismic and acoustic measurements from a series of high-altitude and surface explosions conducted in Kazakhstan recorded at distances of 6, 9.5, and 21 km. Their analysis focused on the modeling of Airy phases that dominate the seismic recordings and successful testing of theoretical work on air-coupled Rayleigh wave excitation. Several studies have investigated local distance seismic ground motions for near-surface explosions. Flynn and Stump (1988) analyzed seismic ground motions for trinitrotoluene (TNT) explosions (W=115 kg) in dry alluvium at depths of 1.8 to 11.5 m, corresponding to scaled DOB (sDOB) of 0.37 to 1.3 m/kg$^{1/3}$, which span the sDOB range of interest for this study. The near-source seismograms

were analyzed at scaled ranges of 3.5 to 46.9 m/kg$^{1/3}$ (closer than this study). They found that P-wave amplitudes increase relative to the fundamental mode Rayleigh wave, Rg, as DOB increases. They also inferred attenuation of P and Rg waves by regressing ground velocity amplitude, A, versus scaled range, $r_s = r/W^{1/3}$ (r is range) following a simple power law: $A \sim r_s^{-b}$., where b = 1.3 and 1.6 for the vertical and radial component P-waves, respectively. They found Rg attenuates less rapidly as expected for a surface wave. Other power-law fits to amplitude data can be found in Medaris (1979) where b ~ 1.4, Gupta and Hartenberger (1981) where b ~ 1.4, and Reamer and Stump (1992) where b = 1.4 and 1.8 for the vertical and radial component, respectively.

The standard measurement in vibration monitoring due to explosions is the peak particle velocity (PPV). Kohler and Fuis (1992) analyzed a USGS database of vertical ground velocity measurements to regress PPV on scaled distance for several media. In their model, distance is scaled by the square-root of yield and PPV is a linear function of both scaled distance and squared scaled distance, so their scaled distance exponents (b from above) cannot be easily compared with other studies. Leidig et al. (2010) abandoned the squared term and analyze PPV from several granite shots where they point out that the use of square-root scaled distance is appropriate when the charge length to diameter is >6. They find b, the scaled distance exponent, to be around 1.6 with little difference when square-root or cube-root scaled distance is employed.

Koper et al. (2002) developed empirical scaling laws for seismic and air-blast amplitudes for surface explosions to estimate yield. They used data from the DIPOLE MIGHT series of explosions at White Sands Missile Range, which was designed to emulate truck bomb explosions

(emplacement just above the ground surface, HOB ~ 1.5 m and W = 3,000 – 12,000 kg TNT-equivalent). These experiments used seismic and overpressure signals spanning the range 1 to 16 km. They investigated several measurements of seismic and air-blast amplitudes in search of robust estimators of yield. Among the measurements considered were: peak P-wave displacement, whole waveform low-frequency level and corner frequency for seismic; and peak overpressure, positive phase impulse and duration and shock velocity for air-blast. They found that air-blast positive phase impulse and duration were good estimators of yield. They also found that seismic whole waveform low-frequency level and peak P-wave displacement and air-blast peak overpressure were also useful in yield estimation.

In this study we use seismo-acoustic signals of low-yield explosions from the Humble Redwood test series spanning a range of near-surface HOB/DOB. These data allow us to develop quantitative models of signal variation with yield, range and HOB. We find that yields of near-surface explosions are best inferred from simultaneous inversion of seismic and overpressure data in order to minimize the emplacement trade-off with yield. In the following sections we will describe the experiments and data sets considered in this study. We will then describe the development of measurements and models for both seismic and air-blast motions. Finally, we will use the models in a simple grid search inversion scheme to illustrate the power of simultaneous inversion of seismic and air-blast data to infer W and HOB. A companion study on more sophisticated stochastic inversion of the seismo-acoustic measurements developed in this study is in preparation (Ramirez et al., manuscript in preparation).

Humble Redwood Experiment

Humble Redwood I and II (HRI/HRII) was a height-of-burst (HOB) and depth-of-burial (DOB) experiment carried out by the Defense Threat Reduction Agency (DTRA) at Kirtland Air Force Base, New Mexico (Foxall et al., 2008; 2010; Marrs et al., 2011). The test site is situated on dry desert alluvium soil with dipping basement structure in the sub-surface. The HRI detonations took place during August and September in 2007 and consisted of seven identical ammonium nitrate and fuel oil (ANFO) charges. Each charge was 1450 lbs and produced an explosive yield of approximately 540 kg TNT equivalent. HRII consisted of six additional detonations in September 2009 with three of them executed as blind tests, where only the project leader (R. Reinke) knew the yield and height-of-burst. A map of the locations with HOB is given in Figure 1, where the blind tests are noted with '?'.

Seismic data and methods

The shots were recorded by 3-component intermediate-period seismometers (Guralp CMG-40T) and short-period geophones (Springnether S-6000) as well as a borehole broadband seismometer (Guralp CMG-3T) at permanent station, ANMO. Locations of the seismic stations are given in Figure 1. A plot of vertical-component motions (ground velocity) of all shots recorded at station E3 (distance approximately 4340 m from the shots) is given in Figure 2. There is a strong correlation between waveforms for all shots, where phase is very consistent and amplitude decreases as HOB increases for the buried shots but is approximately equal for shots above ground (HOB>0). We found similar behavior at other stations where the waveforms are

remarkably similar and the amplitudes increase as HOB decreases below ground. Shots above ground resulted in remarkably similar waveforms including amplitudes.

A record section of shot HRII-4 is given in Figure 3, where there is a large difference in amplitude dependent on station azimuth from the shot. This behavior correlates with thickness of the sedimentary layer above basement rock (Marrs et al., 2011). A close-up of this phenomenon is provided in Figure 4 for shot HRI-F recorded at a station to the west (W1) and east (E3) of ground-zero (GZ) at a distance of approximately 4 km. Waves travelling to stations west of GZ propagate almost entirely through deep low-velocity valley fill, while those to the east are impacted by shallowing bedrock interface. The later-arriving seismic energy plotted in Figure 3 is affected by the very different structure on each side of GZ and the maximum amplitude at station W1 is more than ten times the maximum amplitude at station E3. The difference in structure is evident in a standard shallow explosion analysis that measures vertical peak-particle velocity (PPV) as a function of distance scaled by the square-root of yield (Kohler and Fuis, 1992; Leidig et al., 2011) as is done in Figure 5. This measurement takes the peak particle velocity in the seismogram in the time window between the first P-wave and the air-blast arrival (~330 m/s) and thus impacted by the waveform variability seen in Figure 3. We found that this variability made the low-frequency spectral measurement of Koper et al. (2002) to be highly path-dependent (up to a factor of ten) and an undesirable candidate for a transportable estimator of source properties.

Figure 4, showing the vertical component ground velocity at nearly equidistant stations to the east and west of GZ, suggests that the amplitude of the first P-wave arrival is less affected by the

path-dependent propagation as shown by Figure 3. Site response likely plays a role in the amplification of energy following the very first P-wave for the recordings to the west in the deeper basin structure. Therefore, in the following analysis we will concentrate on this first arrival. Figure 6 shows the first-arrival waveforms as a function of distance and HOB. Note that these first-arriving P-wave velocity records are very simple and remarkably similar across the recording network in both directions. The amplitudes vary slightly less quickly than $1/r^2$ as expected from previously reported studies (e.g. Flynn and Stump, 1988; Reamer and Stump, 1992; Koper et al., 2002), as the scaled amplitudes in this Figure 5 increase with range.

The energy release, or yield, of an explosion is proportional to the mass, or volume, of the explosive. Note that yield includes all forms of energy (thermal, mechanical and radiation). Since the units of volume are length-cubed, the yield (W, given in kg) is proportional to length-cubed, or conversely, length is proportional to the cube-root of yield. Since energy has units of length over time squared, time must also be proportional to the cube-root of yield (Denny and Johnson, 1991). Such hydrodynamic energy relationships have been used to define a power-law distance-dependence of the form, $\delta_s = \delta_0 \cdot r_s^{-b}$, where δ_s is the scaled seismic observable, r_s is the range scaled by the cube-root of yield, $r \cdot W^{-1/3}$, and δ_0 and b are the power-law constants for a reference yield of 1kg or 1 kiloton (kt) (Sauer et al., 1979, Kinney and Graham, 1985). The appropriate scaling of the seismic observable is based on its units, where for example displacement, d, with units of length, is scaled by the cube-root of yield ($d_s = d \cdot W^{-1/3}$) and velocity, u, with units of length over time, is scaled by unity.

We measured the peak displacement, velocity, and acceleration of the first seismic arrival and found the best fit to a power-law scaled distance-dependence was with scaled displacement. Adams et al. (1961) and Murphy and Lahoud (1969) found that of three types of seismic observables, displacement, velocity, and acceleration, only displacement legitimately follows cube-root scaling. They note the reason for this is that outside the hydrodynamic region, in the seismic far-field, the elastic medium introduces other characteristic lengths and a low-frequency observation such as displacement is less susceptible to these effects. Additionally, in a most relevant previous study of surface explosions, Koper et al. (2002) found the peak displacement of the first arrival to be the most robust yield estimate of the observables they tested.

Since the seismic data were a mix of intermediate- and short-period sensors, we normalized all data to the short-period response of a geophone with a corner at 2-Hz, similar to the Springnether S-6000 deployed in HR-I, HR-II and Dipole Might. This is similar to the approach taken for the local magnitude scale in California, where the recorded ground motion is standardized to the response of a short-period Wood-Anderson seismometer for consistency across technological advancements in seismic instrumentation (Uhrhammer et al., 2011). The short-period standardization also allows for wider use of the models developed here since common instrumentation in near-field seismic monitoring is the short-period geophone.

We follow Koper et al. (2002) in our processing of the seismic data. The horizontal components are rotated to radial and transverse and a nominal instrument correction to velocity is made. The data is then convolved with the theoretical response of a geophone with a freeperiod of 0.5 s and a damping of 0.6 (Carver et al., 1986), band-passed with a causal 2^{nd} order Butterworth filter

between 0.5 and 5 Hz, and integrated to displacement. The peak displacement of the first-arrival is measured, the mean noise level is subtracted, and the vertical (d_z) and radial (d_r) measurements are combined to form the geometric mean $d = (d_z^2+d_r^2)^{½}$. An example of the measurement is given in Figure 7 and the scaled-displacement as a function of scaled-distance and scaled-HOB is given in Figure 8.

A major drawback in the use of short-period displacement is the saturation of the measurement at large yields. Using the corner-frequency-yield relationship from Denny and Johnson (1991), an explosion with a yield greater than approximately 10^6 kg (1 kt) will have a source corner frequency less than the 2-Hz corner frequency of the standardized geophone response. In search of a robust yield estimator that is transportable across difference instruments, we also measured the integral of the squared sum of the broadband velocity (using only broadband instruments) of the vertical, radial, and transverse components, $\int\Sigma v^2$. This measurement is proportional to the radiated seismic energy (Kanamori et al., 1993), which is proportional to yield. An example of the measurement is given in Figure 7 and the scaled $\int\Sigma v^2$ as a function of scaled distance and HOB is given in Figure 9. Scaled $\int\Sigma v^2$ is more variable as a function of distance and HOB than scaled displacement, but is less scattered than the PPV measurement.

Seismic model

Figure 8 shows that the logarithmic scaled displacement is a combination of a scaled distance term, r_s, and a scaled HOB, h_s, term. The functional form of the distance term comes from the power-law dependence discussed earlier, which becomes linear after the logarithmic

transformation. The functional form of the HOB term is the hyperbolic tangent (tanh), a sigmoid function, which is similar to the one used to describe coupling as a function of depth-of-burial in Patton and Taylor (2011). The tanh function well describes the behavior for $r_s \gg h_s$, which is the case in this study. At greater $|h_s|$ emplacement (away from the near-source regime considered in this study) an additional term would be needed to account for the added dimension in range. The functional form of our model is then:

$$\log_{10}(d_s) = \beta_1 + \beta_2 \log_{10}(r_s) + \beta_3 \tanh(\beta_4 h_s + \beta_5) \quad (1)$$

where d_s is the scaled displacement [$m \cdot kg^{-1/3}$], r_s is scaled distance [$m \cdot kg^{-1/3}$], and h_s is scaled height-of-burst [$m \cdot kg^{-1/3}$]. If the HOB term in equation (1) were absent the parameters could be estimated via linear regression after logarithmic transformation of d_s and r_s. However, the HOB term makes the equation non-linear and we estimate all parameters via a nonlinear regression (Venables and Ripley, 2010) on the observed logarithmic scaled displacement (left-hand side of equation (1)). The best-fit parameters of equation (1) are given in Table 1. Scaled displacement predictions based on the model presented in equation (1) with the parameters given in Table 1 are shown in Figure 10. Station W5 is not fit well by the distance dependence of the model, probably due to a near-site amplification effect (site response). Also note that shot HRII-6 does is not well fit by the HOB dependence of the model. However, both outliers could be corrected by adding a site- or source-specific constant, as could be done in calibration approach.

Pressure data and methods

The HR shots were recorded by prototype overpressure sensors based on piezoelectric transducers along with modified Validyne diaphragm overpressure sensors (Reinke et al., 2006). The piezoelectric-based sensors deployed in HRI had a limited low-frequency response that was corrected in the deployment for HRII. Locations of the acoustic sensors are given in Figure 1. Several of the sites had co-located seismic and acoustic sensors.

The pressure-time history of HRI-B recorded at a distance of approximately 275 m by a piezoelectric-based sensor at station S20 and by the diaphragm-based sensor (Validyne) at station LV1 is shown in Figure 11. Koper et al. (2002) found the area beneath the positive phase of the airblast measurement, or positive phase impulse per unit area i, (henceforth referred to simply as the impulse) to be a very robust estimator of yield. However, the limited low-frequency response of the piezoelectric-based sensor would bias this measurement low as is evident in Figure 11 when compared with the more broadband Validyne recording. Therefore, we do not use the piezoelectric-based impulse measurements of HRI, but we did include the data from the corrected sensors in our analysis of HRII.

Figure 12 shows the acoustic waveforms recorded at stations LV1, E1, and BRDW. HRII-1 and HRII-3 did not produce an acoustic signal above the noise and are not plotted. The pressure step combined with an exponential decay to a region of underpressure, then return to equilibrium is evident in all the aboveground waveforms. There is some complexity for deeply buried shots. Figure 13 shows the pressure time history of shot HRI-G with an HOB of –5 m (buried 5 m below ground) recorded at a distance of about 275 m at station LV1. Vortman (1965) and Sauer

and Schoutens (1979) observed pressure waveforms from buried explosions similar to that seen in Figure 13, where the first pulse comes is excited when the ground shock strikes the surface and the larger secondary arrival results when the explosion gas products break through the ground surface and a larger pressure source propagates into the atmosphere. These waveforms present a difficulty in the measurement of impulse, where the area of the full positive phase may be much greater than the area attributed to overpressure by the explosion. In this analysis we measure the positive phase area beginning at the most impulsive arrival (hachured area in Figure 13) for the calculation of impulse.

The same yield scaling considerations discussed in terms of the seismic observables also hold for overpressure measurements with the added scaling due to variable air density. For example, the volume of a sphere needed to contain a given amount of energy is larger at higher altitudes where the air is thinner. Because volume is inversely proportional to air density, it is necessary to scale pressure by the ambient pressure and time is scaled by ambient pressure and temperature (Dolan, 1972). The scaled impulse i_s is then the impulse scaled by the cube-root of yield, the square of the cube-root of pressure, and the inverse square-root of temperature, where $i_s = i \cdot W^{-1/3} (P/P_0)^{-2/3} (T/T_0)^{1/2}$, where P and T are the ambient pressure and temperature and P_0 and T_0 are standard pressure (101325 Pa) and temperature (288°K) at sea-level. Range is scaled by the inverse cube-root of pressure in addition to the cube-root of yield, $r_s = r \cdot W^{-1/3} (P/P_0)^{1/3}$. Observations of scaled impulse versus scaled distance and HOB are plotted in Figure 14.

Figure 11 also shows observations of peak pressure, which is the other acoustic measurement used to estimate yield in this study. Both types of sensors record similar peak pressures, but the

high-frequency response of the instrument is unable to capture the step in pressure so that the peak pressure measurement is biased low. In order to compensate for this effect and find the true peak pressure, p_0, we model the decay of the pressure with an exponential function of the form

$$p(t) = p_0(1-t_r)\exp(-b\,t_r) \tag{2}$$

(Smith, 1995), where t_r is equal to the time scaled by the positive phase duration, t_{dur} ($t_r = t/t_{dur}$), and b is a decay constant fit to the pressure decay between its peak and trough (Figure 11). We use this method rather than a fit to the log-linear portion of the positive phase since at small pressures there are too few points for an appropriate extrapolation to peak pressure. Scaled pressure p_s is the pressure scaled by the ambient pressure ratio, where $p_s = p\,(P/P_0)^{-1}$. Observations of scaled pressure versus scaled distance and HOB are plotted in Figure 15.

Pressure model

Figure 14 shows that similar to the seismic observations, the logarithmic scaled impulse is a combination of a scaled distance term, r_s, and a scaled HOB, h_s, term. The functional form of the distance term comes from the spherical spreading of the blast wave and can be described by a power-law, $r^{-\alpha}$, which becomes linear after the logarithmic transformation. The functional form of the HOB term could be fit with a sigmoid function similar to the hyperbolic tangent used in the seismic analysis, but this is unsatisfactory for two reasons as illustrated in Figure 16 (dashed line in right panel). The first is a theoretical consideration since as the explosion is buried deeper there is less energy transferred to the break the surface, so overpressure should go to zero. The

second reason is that a fit to the data in Figure 14 would produce a tanh function that flattens out at $h_s < 0.7$, which would predict an observation of HRII-3 (HOB = –10 m) at station LV1 of approximately 0.4 Pa-s that is not seen. We note that the noise floor at this distance is approximately 0.005 Pa-s - almost two orders of magnitude below the predicted observation so the observation wouldn't be hidden by noise. Therefore, we choose a function of HOB that asymptotically approaches zero for deeply buried shots. The final model is then

$$\log_{10}(i_s) = \beta_1 + \beta_2 \log_{10}(r_s) + \beta_3 h_s - \frac{1}{10}\log_{10}(1 + 10^{10\beta_3 h_s}), \quad (3)$$

where i_s is the scaled impulse, r_s is scaled distance, and h_s is scaled height-of-burst ($h_s = h \cdot W^{-1/3} (P/P_0)^{1/3}$). We estimated the parameters in equation (3) via a nonlinear regression on the observed logarithmic scaled impulse, similar to our seismic model. The best-fit parameters of equation (3) are given in Table 2. Note that the distance dependence that results from regression is –1, which is predicted for spherical spreading. Scaled impulse predictions based on the model presented in equation (3) with the parameters given in Table 2 are shown in Figure 16. There is still some suggestion from the more deeply buried shots that the impulse goes to zero more gently than afforded by the HOB term in equation (3) and this will have to be the subject of future work. The zero-slope at HOB>0 has also been seen in HOB nuclear weapons tests (Cockayne and Lofgren, 1976).

Figure 15 shows that peak pressure can be modeled with the same functional form as given in equation (3). A comparison with the impulse plotted in Figure 14 shows that pressure is much more variable as a function of distance and HOB than impulse. In addition, Koper et al. (2002)

found impulse to be the most robust predictor of yield. For these reasons, we choose to concentrate on impulse in the following analyses.

Discussion

The analyses of seismic and overpressure signals from near-surface explosions show that the scaled seismic P-wave displacement and air-blast impulse provide the diagnostics of yield (W) and height-of-burst (HOB). The quantitative models developed above clearly indicate that the estimation of yield for explosions with unknown emplacement (HOB) is non-unique – the amplitudes of seismic and overpressure recordings at a given range depend on both yield and HOB. Thus combined analysis of seismic and overpressure data is necessary for a more robust estimation of yield when HOB is unknown. As shown by Figure 10 and the coefficient b_3 in equation (1) as given in Table 1, displacement-predicted yield can vary by a half order of magnitude depending on the HOB. The effect of HOB on seismic and overpressure observations is complementary - at a given range the effect of an increase/decrease in HOB results in an increase/decrease of overpressure amplitude and a decrease/increase of seismic amplitude. A combined inversion of the seismic and overpressure data using the nonlinear multivariate models can estimate both yield and HOB. Although there is little resolution in HOB for above ground tests due to the flattening of both models for HOB>0 (Figures 10 and 16), the inversion can still provide a constraint on yield, and good estimates of both yield and HOB should be possible for near-surface (HOB~0) and buried (HOB<0) explosions. In the following sections we test the efficacy of our signal models for estimating W and HOB.

Test 1: Dipole Might and Divine Buffalo

A series of controlled vehicular explosions named Dipole Might (DM) and Divine Buffalo (DB) were carried out at the White Sands Missile Range, New Mexico. More details of the four explosion tests can be found in Koper et al. (2002). We measured the displacements and impulses of the combined DM/DB dataset and compared them in a scaled sense with the HR observations in Figure 17. The DM/DB observations compare well with the predictions for an HOB of 1.5 m, approximately the height of the truck bed used in the experiment.

The favorable comparison is not surprising since the tests were conducted in similar geologic environments (dry alluvium). Figure 17 also compares the observations to the seismic and acoustic models reported by Koper et al. (2002). The Koper et al. (2002) models do not explicitly include HOB, so if we transform their simplified model $W = d \cdot r^2$ to scaled mks units and put it in the log-linear form of the first distance term in equation (1) we obtain $b_1 = -3$ and $b_2 = -2$.

If we transform their impulse model (equation (12), Koper et al., 2002) to scaled mks units and put it in the log-linear form of the first distance term in equation (3) we obtain $b_1 = 2.73$ and $b_2 = -1.12$. Finally, we note that the Coppens and Reinhardt (1993) impulse model compares well with the observations when the factor of two correction is used for surface shots. If we transform the Coppens and Reinhardt (1993) model (equation (11), Koper et al., 2002) with the factor of two to scaled mks units and put it in the log-linear form of the first distance term in equation (3) we obtain $b_1 = 2.5$ and $b_2 = -1.0$ (r_s>1m).

Using the models given in equations (1) and (3) with the coefficients in Tables 1 and 2 we can invert the seismic displacements and air-blast impulses measured at a given distance from the DM/DB shots and estimate the yield and HOB. The simplest approach is a grid-search, where the forward solution for a range of yield-HOB combinations at each observation distance is calculated and a $\log_{10}$ residual (observed-predicted) obtained. The median residual of all observations at each yield-HOB point is calculated and the absolute minimum residual for all yield-HOB points in the grid will trace along the yield-HOB trade-off described in equations (1) and (3) for each model.

Results of this grid search are shown in Figure 18. The best-case scenario is displayed in Figure 18 for the DM-21 explosion, where the best-fit to the data from both models intersect at a given yield-HOB point. In this case the intersection of the two yield-HOB curves provides the solution. When the two curves do not intersect, as is the case for DM-22 as shown in Figure 18, a weighting must be applied to the residuals (or to the datasets) in order to combine the seismic and overpressure datasets in a joint inversion. Fortunately, as shown in Figure 17, the datasets have roughly the same range and error in the logarithm domain so we simply sum the absolute residuals from both models at each yield-HOB point in the grid-search and find the global minimum.

Figure 18 shows the other three tests in the DM/DB series for which we have data. Error in yield is less than ±30% and the HOB is most often over-predicted by an average of ~2 m, which is on the order of the diameter of a spherical charge at the DM yields. Both models do not change

much for HOB > 2 m and there is little resolution in the solution near and above this HOB. Finally, we note there is only one seismic and acoustic measurement of DM-22 and the seismic measurement is made at station MCDR (r_s~200 m), which may have a site response issue (Figure 17). Note that this approach assumes the location of the explosion is known so that each distance to the observation is known. The impact of measurement and models errors will be the subject of further investigations.

Test 2: HRII-4

Of the HR blind tests (noted by '?' in Figure 1), HRII-1 did not produce an acoustic signal above the noise, and HRII-2 has only three acoustic observations all with low signal-to-noise ratio (Figure 12), so we estimate the yield and HOB of HRII-4. The same grid search approach as described in the DM/DB section is used to find that the best-fit yield and HOB for HRII-4 is 620 kg at –0.5 m, respectively (Figure 19). Figure 19 shows that using only seismic or acoustic data results in a goodness of fit curve where yield and hob trade-off (black and gray curves for seismic or acoustic only grid search, respectively). This trade-off is only broken when both data sets are used to predict the yield and HOB. In order to get at an estimate of error we normalize the residuals of each dataset by the standard deviation σ of the $\log_{10}$ error in the fit to the data of the HR shots with known yield and HOB - the training dataset used to define the models. The displacement (seismic) model σ = 0.07 and impulse (acoustic) model σ = 0.09. With these scaled residuals from the grid-search and an assumption of normally distributed error, we can map out a confidence region for the solution as shown in Figure 19.

Subsequent to running our estimate we learned the ground truth parameters for this explosion: W = 754 kg and HOB = -0.6 m. This indicates that we estimated the yield with an error of 18 % and we correctly inferred emplacement below ground. It is encouraging that the ground truth W-HOB lies within the intersection of misfit regions for seismic and overpressure. Nonetheless, improvements over this simple grid search approach can be made. A better approach to this nonlinear multivariate problem is to use a stochastic inversion such as a Markov-chain Monte Carlo (MCMC) solver (Rodgers et al., 2011; Ramirez et al., manuscript in preparation). This approach could better incorporate data and model error, as well as censored data (observations hidden by the noise). The grid-search approach presented here cannot make use of impulse or peak pressure that is below the noise, but such censored data could provide information that the explosion is either deeply buried and/or of small yield when used in combination with seismic data.

Seismic efficiency of the HR explosions

In this section we investigate the efficiency of mechanical motions excited by the near-surface HUMBLE REDWOOD explosions. Kanamori et al. (1993) showed that the seismic energy E radiating from the focal sphere of an earthquake is:

$$E = \rho_0 \alpha_0 \int_{S_0} \int \sum v_0^2 dt\, dS \,, \tag{4}$$

where ρ_0 and α_0 are the density and compressional velocity of the medium at the focal sphere, the surface integral is taken over the focal sphere, and the integration with time is to be taken

over the P-wave. The term $\sum v_0^2$ represents the squared sum of the velocity of the vertical, radial, and tangential components. Furthermore, the velocity observed at some range r can be used to estimate the velocity on the focal sphere v_0 using the relation $v = v_0 A\ q(r)/q(r_0)$ where r_0 is the radius of the focal sphere, A is the free-surface amplification = 2, and $q(r)$ is a loss function incorporating spreading, attenuation, and scattering.

We define the loss function as $q(r) = r^{-1}\exp(-\pi f r/\alpha Q)$, where the inverse range term is due to spherical spreading and the exponential term is due to attenuation Q along the path. Q and α are estimated from the distance dependence coefficient ($\beta_2 = -1.74$) in equation (1) by performing a grid-search over possible Q and α and finding the best fit to the distance dependence. Figure 20 shows the results of the grid-search where we choose $Q = 10$ and $\alpha = 1100$ m/s from the plausible choices which offer a good fit to the distance dependence (Figure 20, right panel).

We add an additional loss term, $C(h)$, that is a seismic coupling function dependent on HOB h, so that v is now:

$$v = v_0\, C(h)\, A\, q(r)/q(r_0) \tag{5}$$

C(h) is estimated from the third HOB-dependent term in equation (1) and given in Figure 21. Rearranging equation (5) to solve for v_0, inserting it in to equation (4), and integrating along the surface of the focal sphere gives:

$$E = 4\pi r^2\, C(h)^{-2}\, A^{-2}[r_0\, q(r_0) / r\, q(r)]^2\, r_0\, \alpha_0 \int \Sigma v^2\, dt \tag{6}$$

we set r_0 = 1 m, and assume ρ_0 = 1600 kg/m^3 (Koper et al., 2002) and $\alpha_0 = \alpha$ (compressional velocity is same at source and receiver). $\int \Sigma v^2$ was calculated as part of the broadband analysis described in the seismic data analysis section, which we use to estimate the radiated seismic energy and divide it by the energy contained in the explosive to obtain a ratio of radiated to explosive energy (540 kg × 4.184 MJ/kg TNT), or the seismic efficiency. The distribution of seismic efficiency measured in the HR experiment is shown in Figure 22, where the median seismic efficiency is near 1% and the range is ½-2%.

Haskell (1967) derived radiated seismic energy from calculated seismic reduced velocity potentials of explosions and found the ratio of radiated to explosive energy to be between 1 and 5% based on the medium, where the lowest ratios were for alluvium. From a survey of radiated seismic energy studies, Rodean (1971) concludes that less than 10% of the explosion energy is available to generate seismic waves, and Koper et al. (1999) used a seismic efficiency of 3% in their analysis of the Nairobi explosion.

Conclusion

In this study we measured features from seismic and overpressure recordings of near-surface explosions conducted in the Humble Redwood I and II test series. We considered several measurements and found that the zero-to-peak vector displacement of the seismic P-wave and the impulse of the overpressure signals provide the least scatter and desirable sensitivity to yield and height-of-burst (HOB). We developed algebraic models for these measurements that can

easily be used to estimate yield and HOB. The use of both seismic and overpressure measurements allow for the trade-off between yield and height-of-burst to be constrained. When compared with explosions of known yield and HOB we find the predictions of the model are within ±30% of the yield and a factor of 2 for HOB. In all cases considered here, we were able to obtain the correct sign of the HOB (above or below ground). The integral of seismic velocity-squared can be used to estimate seismic energy and we find the median seismic efficiency of the HR explosions is near 1%.

The methodology presented in this study provides a quantitative description of seismic and overpressure amplitudes for explosions near the Earth's surface. These models can be used to investigate explosion yield and emplacement as part of forensic analysis of explosions. Because of the strong trade-off between signal amplitude and the yield and HOB/DOB clearly both seismic and overpressure data must be used to provide best possible estimates. While the current study used data from an idealized set of experiments in the same geologic material, clearly additional factors can complicate observed seismoacoustic signals and bias the amplitudes and subsequent W and HOB estimates. For example, the effect of material strength is known to strongly impact seismic amplitudes for deeply buried explosions (e.g. Perret and Bass, 1975) and these effects should be investigated to expand the applicability of our signal models to other geologies. Future experiments and/or numerical simulations of ground motions and overpressures may provide predictions of blast-generated motions and insights into dependence on material properties. Further complications could arise from near-source structure, such as vehicles or buildings. While these complications remain to be investigated, this study establishes

the basic phenomenology of local distance seismoacoustic energy partitioning for near-surface explosions.

Data and Resources

The data used in this study from the Humble Redwood –I and –II experiments is available to others for research purposes. Requests should be sent to the A. Rodgers. Data from Dipole Might/Divine Buffalo experiments were provided by Dr. Keith Koper and requests for these data should be directed to him. Plots were made using the Generic Mapping Tools version 4.2.2 (www.soest.hawaii.edu/gmt; last accessed 8 April 2002). Seismic analysis was done with Seismic Analysis Code version 7.10.5 (www.iris.edu/sac; last accessed 8 April 2011).

Acknowledgements

We are grateful to Pat Lewis (LLNL), Doug Seastrand (NSTec) and Al Leverette (DTRA) for field deployment of sensors, data collection and reduction. This study benefited from earlier analysis of overpressure data by Ross Marrs (LLNL). Keith Koper kindly provided the Dipole Might/Divine Buffalo data set. Funding for this study was provided by the U.S. Department of Energy's NNSA, Office of Defense Nuclear Nonproliferation Research and Development and the Defense Threat Reduction Agency. The authors thank Dr. Tom Kiess and Dr. Phil Cole for their support of our efforts. This research was performed in part under the auspices of the U.S. Department of Energy by the Lawrence Livermore National Laboratory under contract number DE-AC52-07NA27344. This is LLNL contribution LLNL-JRNL-635120.

References

Adams W. M., R. G. Preston, P. L. Flanders, D. C. Sachs, and W. R. Perret (1961), Summary report of strong-motion measurements, underground nuclear detonations, *J. Geophys. Res*., 66, 903-942.

Arrowsmith, S. J., J. B. Johnson, D. P. Drob, and M. A. H. Hedlin (2010), The seismoacoustic wavefield: A new paradigm in studying geophysical phenomena, Rev. Geophys., 48, RG4003, doi:10.1029/2010RG000335.

Bonner, J., R. Waxler, Y. Gitterman and R. Hofstetter, Seimo-acoustic energy partitioning at near-source and local distances from the 2011 Sayarim explosions in the Negev Desert, Israel, *Bull Seismo. Soc. Amer*., 103 (2), 741-758.

Carver, D. L., D. R. Cunningham, and K. W. King (1986), Calibration and acceptance testing of the DR-200 digital seismograph with S-6000 and L-4C seismometers, USGS OFR 86-340.

Cockayne, J. E. and E. V. Lofgren (1976), Tactical implications of air blast variations from nuclear weapon tests, SAIC SIA-76-677-WA, DNA Contract 001-76-C-0284, DTIC number A048802.

Coppens, A. B., and R. A. Reinhardt (1993). Explosives and Explosions, Naval Postgraduate School, Monterey.

Denny, M. D. and L. R. Johnson (1991), The explosion seismic source function: Models and scaling laws reviewed, in Explosion Source Phenomenology, eds. Taylor S. R. et al., AGU Monograph 65: 1–24.

Dolan, P. J. (ed.) (1972), Capabilities of Nuclear Weapons, DNA-EM-1, Part I Phenomenology, Defense Nuclear Agency, Washington, D.C.

Flynn, E. C. and B. W. Stump (1988), Effect of depth on near-source seismograms, J. Geophys. Res., 93, 4820-4834.

Foxall, B. R., R. Reinke, C. Snelson, D. Seastrand, R. Marrs, O.R. Walton, and A.L. Ramirez (2008). The HUMBLE REDWOOD Seismic/acoustic coupling experiments (abstract), Seismo.. Res. Lett., 79.

Foxall, B., R. Marrs, E. Lenox, R. Reinke, D. Seastrand, J. Bonner, K. Mayeda, and C. Snelson (2010). The HUMBLE REDWOOD seismic/acoustic coupling experiments: Joint inversion for yield using seismic, acoustic, and crater data (abstract), Seismol. Res. Lett. 81, 315.

Gupta, I. N., and R. A. Hartenberger (1981). Seismic phases and scaling associated with small high-explosive surface shots, Bull. Seism. Soc. Am., 71, 1731-1741.

Haskell, N. A. (1967), Analytic approximation for the elastic radiation from a contained underground explosion, J. Geophs. Res., 72 (10), 2583-2587.

Kanamori, H., J. Mori, E. Hauksson, T. H. Heaton, L. K. Hutton, and L. M. Jones (1993), Determination of earthquake energy release and M_L using TERRASCOPE, Bull. Seis. Soc. Amer., 83 (2), 330-346.

Kinney, G. F., and K. J. Graham (1985), Explosive Shocks in Air, 2nd Ed., Springer-Verlag, New York.

Kitov, I. O., J. R. Murphy, O. P. Kusnetsov, B. W. Barker, and N. I. Nedoshivin (1997), An analysis of seismic and acoustic signals measured from a series of atmospheric and near-surface explosions*, Bull. Seis. Soc. Amer*., 87 (6), 1553-1562.

Kohler, W. M. and G. S. Fuis (1992), Empirical dependence of seismic ground velocity on the weight of explosives, shotpoint site condition, and recording distance for seismic-refraction data, Bull. Seis. Soc. Amer. (82) 5, 2032-2044.

Koper, K. D., T. C. Wallace, R. E. Reinke, and J. A. Leverette (2002), Empirical scaling laws for truck bomb explosions based on seismic and acoustic data, Bull. Seis. Soc. Amer., 92(2), 527-542. doi: 10.1785/0120000242.

Leidig, M., J. L. Bonner, T. Rath, and D. Murray (2010), Quantification of ground vibration differences from well-confined single-hole explosions with variable velocity of detonation, Int. J. Rock Mech. Min., 47(1), 42-49, doi: 10.1016/j.ijrmms.2009.07.006.

Marrs, R. E., R. Reinke, D. Templeton, W. Foxall, E. Lenox, K. Mayeda, J. Bonner, D. Seastrand, A. J. Rodgers (2011). Local To Near-Regional Seismic And Acoustic Signals From Fully Contained, Cratering And Height Of Burst Explosions, Seismo. Res. Lett. (Vol. 82, No. 2).

Medearis, K. (1979). Dynamic characteristics of ground motions due to blasting, Bull. Seism. Soc. Am., 69, 627-639.

Murphy, J. R. and J. A. Lahoud (1969) Analysis of seismic peak amplitudes from underground nuclear explosions, Bull. Seis. Soc. Amer., 59 (6), 2325-2341.

Murphy, J. R. (1996), Types of seismic events and their source descriptions, in Monitoring a Comprehensive Test Ban Treaty, edited by E. S. Husebye and A. M. Dainty, pp. 225–245, Kluwer Acad., Dordrecht, Netherlands.

U.S. Congress, Office of Technology Assessment (1989). *The Containment of Underground Nuclear Explosions,* OTA-ISC-414, U.S. Government Printing Office, Washington, DC.

Patton, H. J. and S. R. Taylor (2011) The apparent explosion moment: Inferences of volumetric moment due to source medium damage by underground nuclear explosions, J. Geophys. Res. 116 (B03310), doi:10.1029/2010JB007937.

Perret, W. R. and R. C. Bass (1975) Free-field ground motion induced by underground explosions, Sandia Laboratories Report, SAND74-0252.

Reamer, S. K. and B. W. Stump (1992). Source parameter estimation for large, bermed, surface chemical explosions, Bull. Seism. Soc. Am., 82, 406-421.

Reinke, R., A. Leverette, and C. Hayward (2006). On the use of differential pressure gauges for low pressure blast measurements, in Proceedings of the 19th International Symposium on the Military Applications of Blast and Shock, Calgary, Alberta.

Rodean, H. C. (1971), Nuclear-explosion Seismology, USAEC Division of Technical Information, Oak Ridge.

Rodgers, A. H. Xu, D. C. Templeton, A. L. Ramirez, V. Chipman, S. R. Ford and D. H. Chambers (2011). Estimation of Yield and Height-of-Burst for Near-Surface Explosions from Joint Inversion of Air-Blast and Seismic Data (Abstract S42A-08), American Geophysical Union Fall Meeting, San Francisco, CA

Sauer, F. M., J. E. Schoutens, W. R. Perret, and R. C. Bass (1979), Ground motion from underground explosions, in Nuclear Geoplosics Sourcebook, Volume IV, Part I, Chapter 2, DNA 6501H-4-2.

Sauer, F. M., and J. E. Schoutens (1979), Ground motion from above ground explosions, in Nuclear Geoplosics Sourcebook, Volume IV, Part I, Chapter 1, DNA 6501H-4-2.

Smith, P.D. (1995), Blast loading, in Blast Effects on Buildings, eds. Mays, G. C. and P. D. Smith, Thomas Telford Publications, London.

Uhrhammer, R. B., and E. R. Collins (1990) Synthesis of Wood-Anderson seismograms from broadband digital records, Bull. Seis. Soc. Amer. 80 (3), 702-716.

Uhrhammer, R. A., M. Hellweg, K. Hutton, P. Lombard, A. W. Walters, E. Hauksson, and D. Oppenheimer (2011), California Integrated Seismic Network (CISN) local magnitude determination in California and vicinity, Bull. Seis. Soc. Amer., 101, 2685-2693, doi:10.1785/0120100106.

Venables, W. N. and B. D. Ripley (2010), Modern Applied Statistics with S, Springer Science+Business Media Inc., New York.

Vortman, L. J. (1965) Ari-blast suppression as a function of explosive charge burial depth, J. Acoust. Soc. Am. **40**, 229 (1966)

Tables

Table 1. Equation (1) parameters

Coefficient	Value
β_1	−3.39(5)
β_2	−1.74
β_3	−0.22
β_4	4.84
β_5	1.23

Table 2. Equation (3) parameters

Coefficient	Value
β_1	2.48
β_2	−1.00
β_3	2.15

Figures

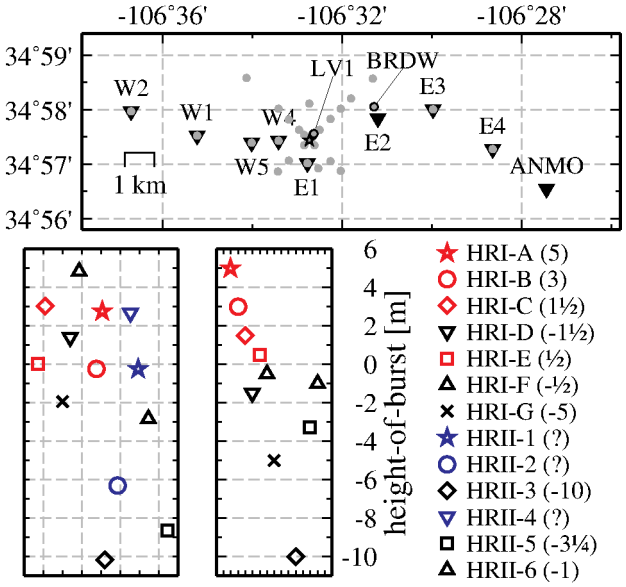

Figure 1. Source-station geometry of the Humble Redwood experiments. The inverted triangles are the labeled seismic stations and the gray circles are the acoustic stations, where LV1 and BRDW are labeled and discussed in the text. The star on the station map is the location of the shots and the inset map shows the shot map where the grid is 10 × 10 m. The lower central panel depicts the height-of-burst (HOB) distribution of the shots. The legend gives the shot name and the HOB in parenthesis, where '?' is a blind test.

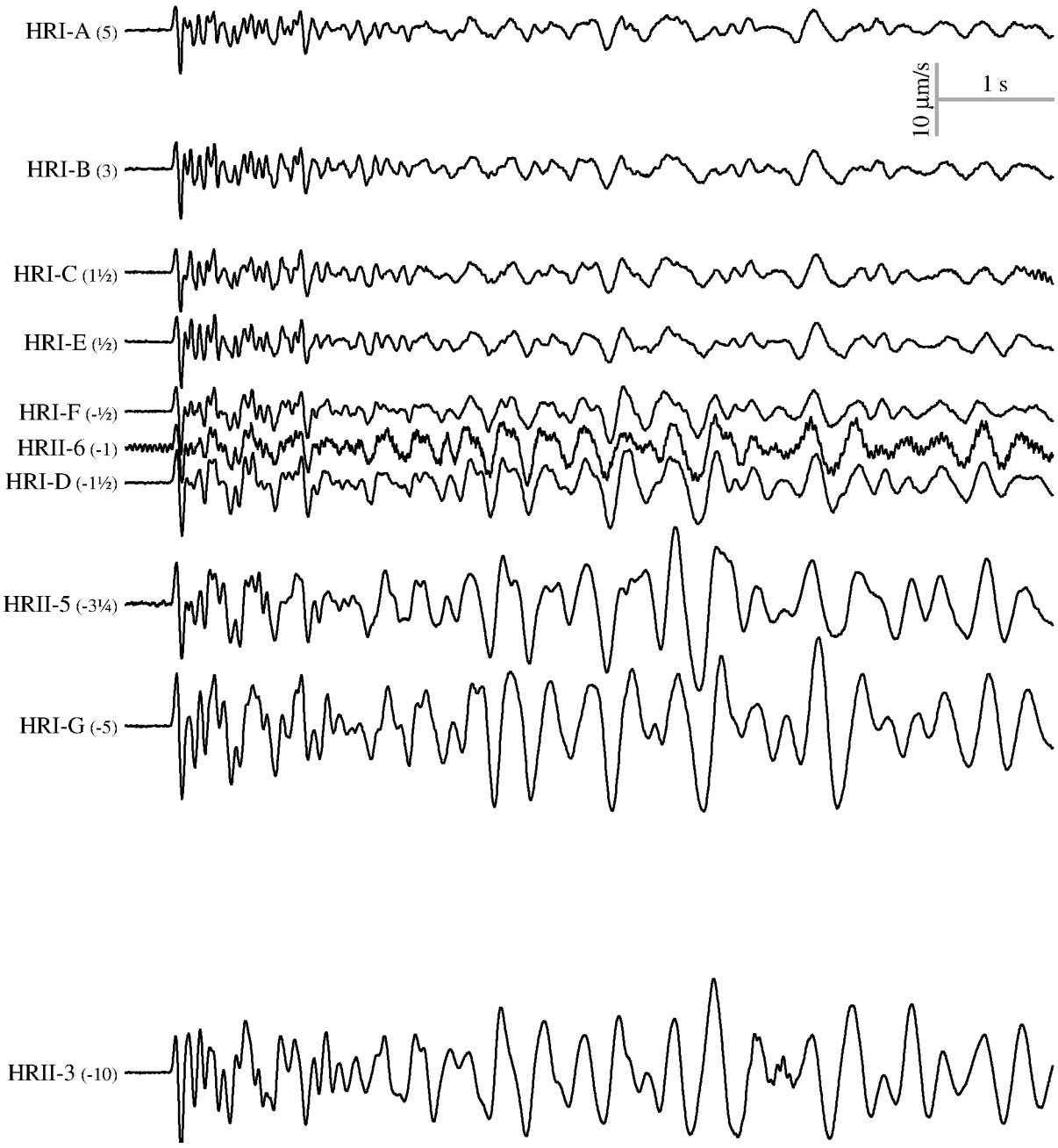

Figure 2. Waveforms recorded at station E3, which is approximately 4340 m from the shots. The shot name with HOB [m] given in parenthesis is listed to the left of each trace. Time and amplitude scales are given in the top-right.

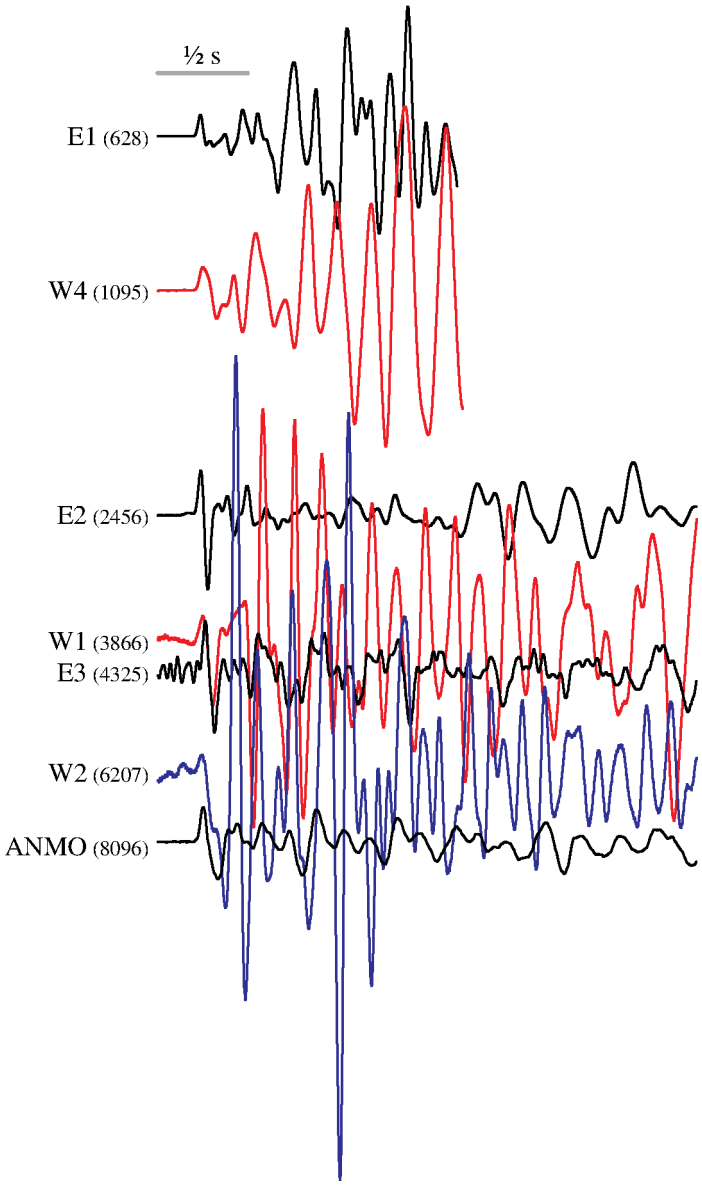

Figure 3. Waveforms from shot HRII-4 where traces are cut before the acoustic arrival and scaled by distance-squared. The station name with distance [m] given in parenthesis is listed to the left of each trace. Traces from stations to the west and east of the shots are red and black, respectively. The recording at W2 is blue for clarity. Time scale is given at the top.

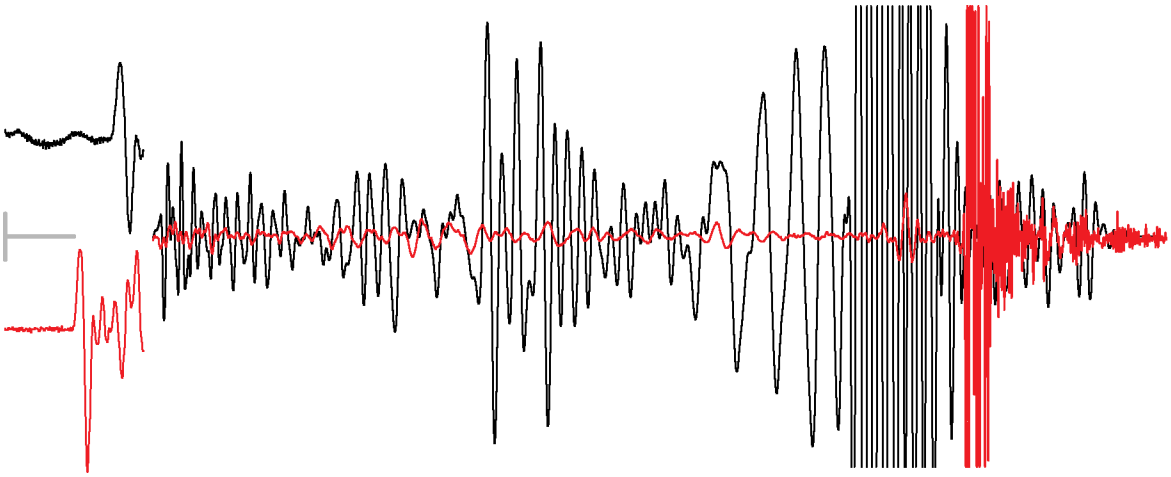

Figure 4. HRI-F recorded at W1 (black) and E3 (red), at a distance of 3788 and 4333 m, respectively. The traces are separated after the first arrival, which is magnified relative to the rest of the trace. The horizontal gray bar is 0.4 or 1 sec and the vertical gray bar is 4 or 20 μm/s for the first and second segment of the waveform, respectively, and the trace begins 1 sec after the origin time. The large amplitude phases are due to acoustic-coupling of the airblast and are clipped for the figure. Note that the ratio of the peak amplitudes from origin time to just before the acoustic arrival is ~12 whereas the ratio of the first arrival peak is ~1.

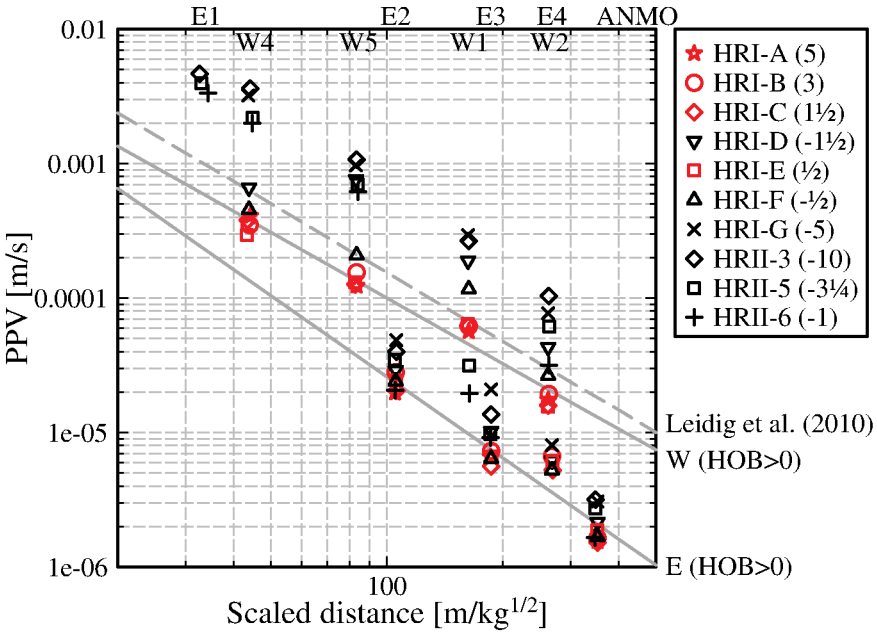

Figure 5. Broadband vertical peak-particle velocity (PPV) versus scaled-distance. Station E4 uses a short-period PPV. Best-fit lines for shots above ground to the west (W) and east (E) are given, as well as that predicted by the granite model of Leidig et al. (2010).

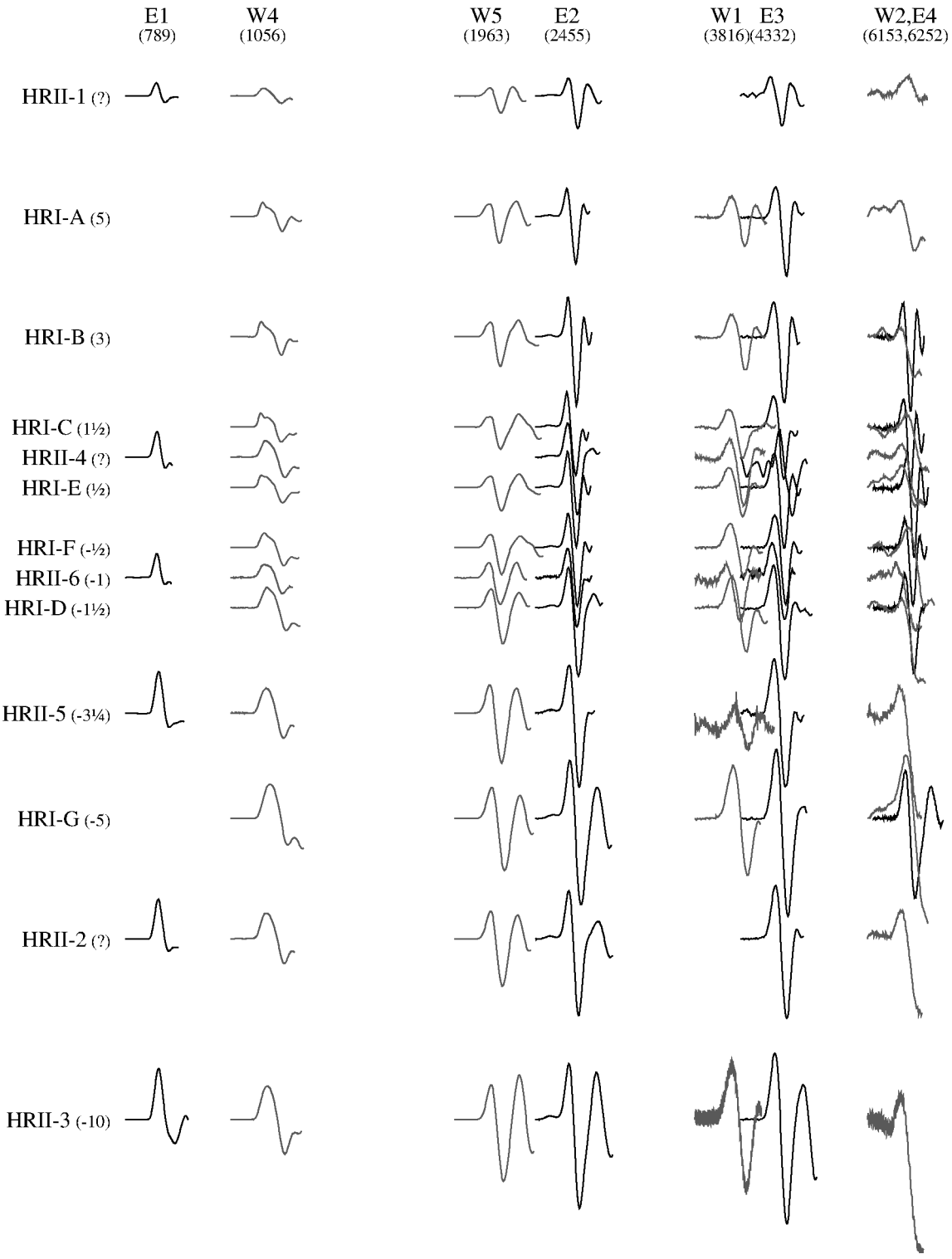

Figure 6. Seismic waveforms organized by HOB and scaled distance, and the amplitude is scaled by distance-squared. Distance [m] and hob [m] for each station or shot are given in parenthesis. W5 is scaled by $1/2\pi$. The gray bar is 0.1 sec long. Stations to the west of GZ are in dark gray and stations to the east are in black.

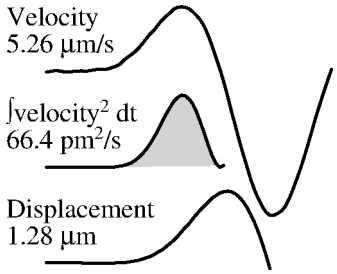

Figure 7. Seismic measurements. The top trace is the nominally corrected velocity where the first-peak value is given. The middle trace is the velocity-squared where the shaded region shows the integral used in the measurement, which is given. The bottom trace is the displacement where the first peak value is given. This data is the vertical trace from HRII-3 recorded at station E3. The trace is 0.2 s long.

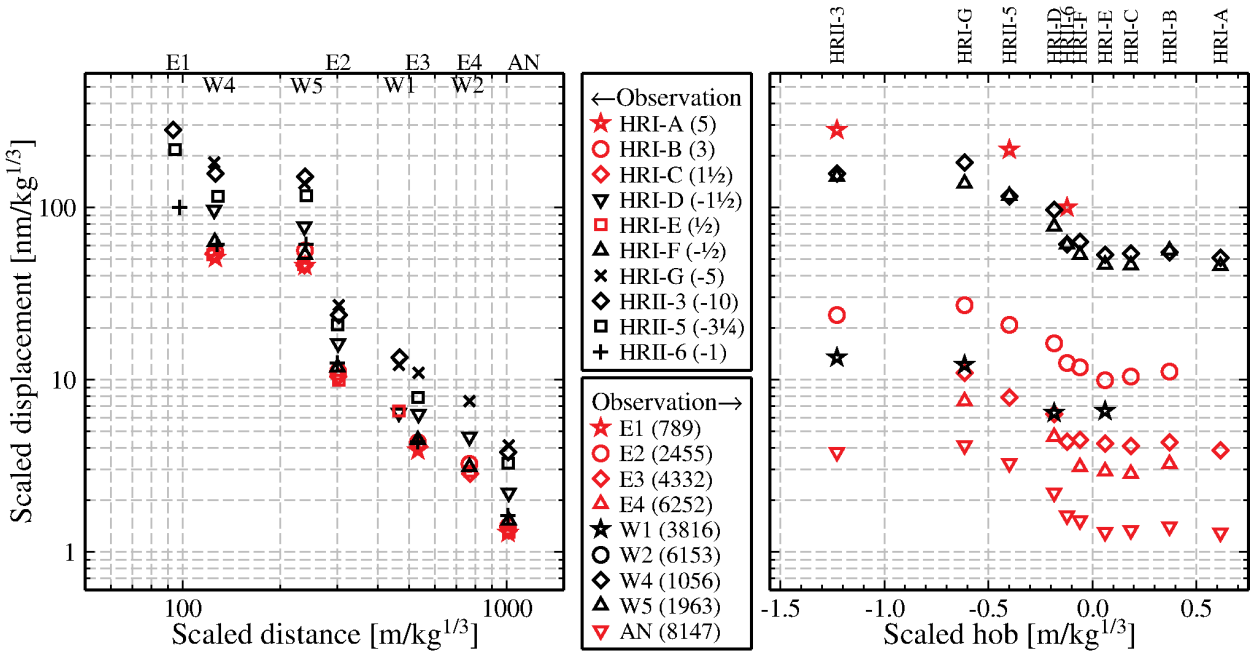

Figure 8. Scaled displacement versus scaled distance (left) and hob (right). The symbols represent the shots in the left panel (red are above-ground and black are below-ground), and stations in the right panel (red are to the east and black are to the west). The stations are labeled at their approximate distance at the top of the left panel and the shots are labeled at their hob at the top of the right panel.

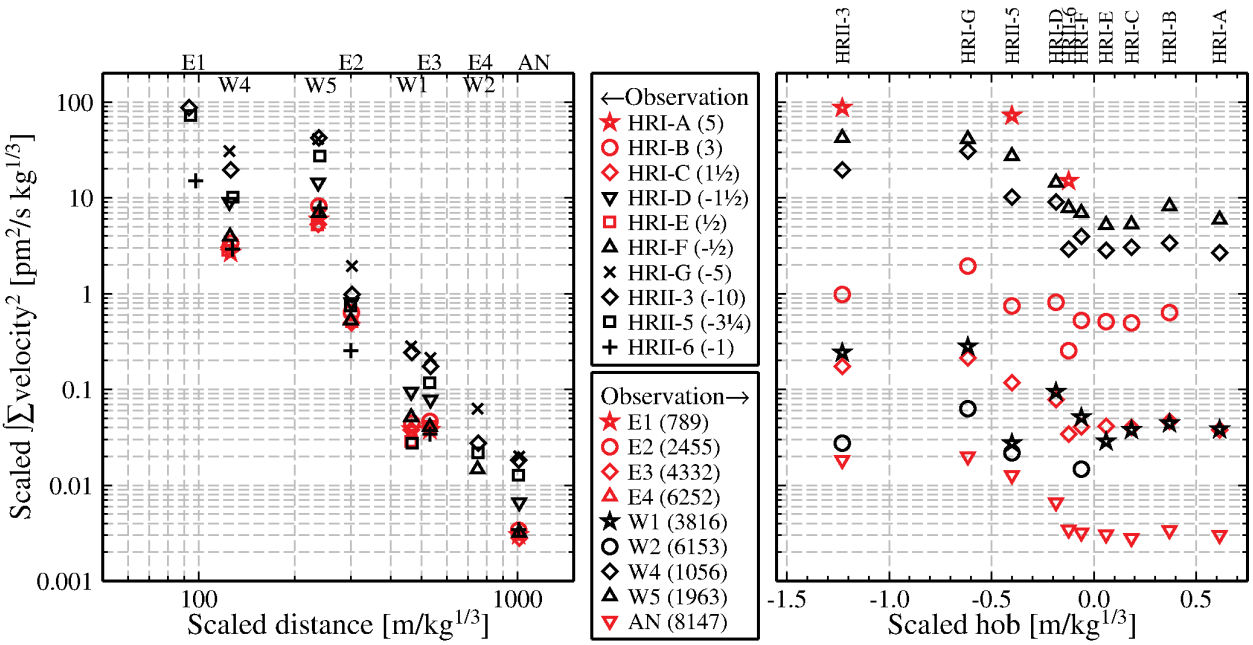

Figure 9. Scaled integral of velocity-squared versus scaled distance (left) and hob (right). The symbols represent the shots in the left panel (red are above-ground and black are below-ground), and stations in the right panel (red are to the east and black are to the west). The stations are labeled at their approximate distance at the top of the left panel and the shots are labeled at their hob at the top of the right panel.

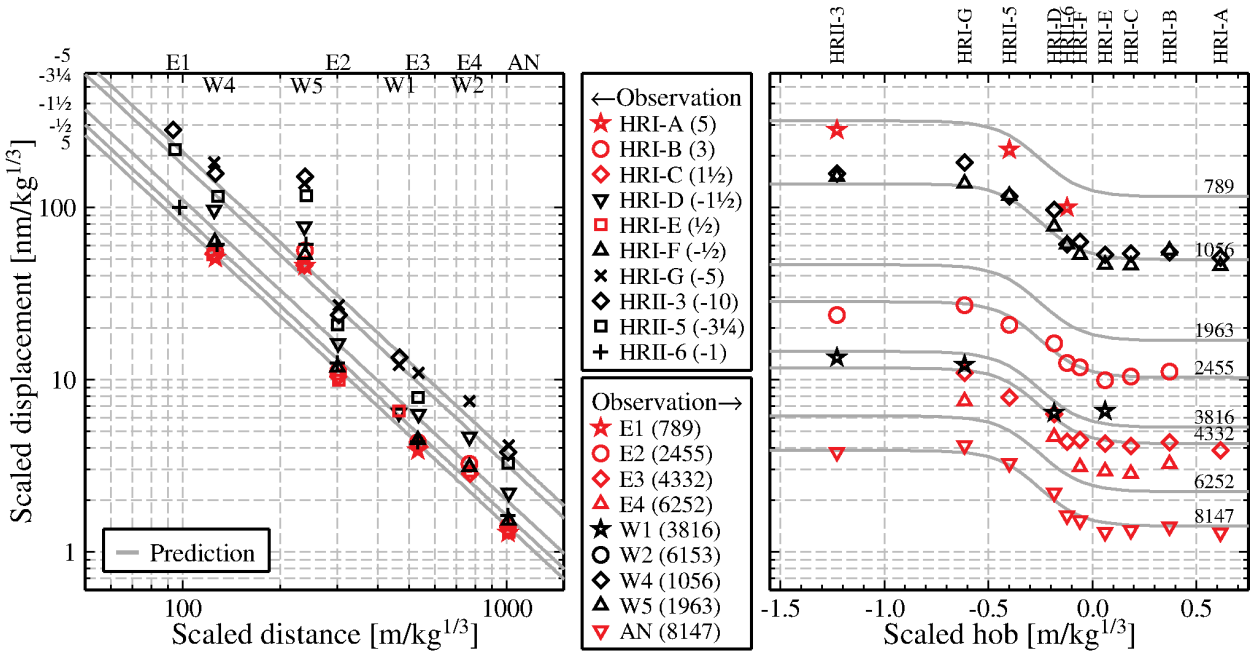

Figure 10. Same as Figure 8 but with predictions (gray lines) based on Equation (1) with parameters in Table 1. The HOB in meters used to make the predictions in the left panel are given at the top-left. The distances in meters (average to each station) used to make the predictions in the right panel are given to the right of each line.

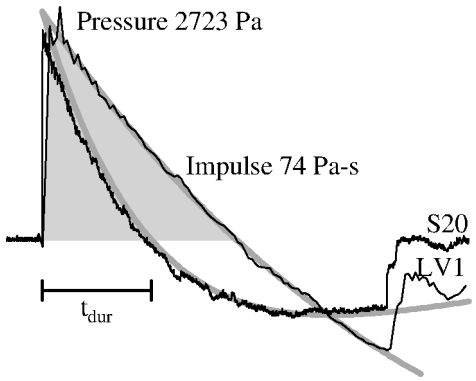

Figure 11. Acoustic measurements of HRI-B. The trace is 0.13 s long. S20 is a piezoelectric-based sensor recorded at 10^4 sps and LV1 is a diaphragm-based (Validyne) sensor recorded at 10^3 sps. Due to the limited low-frequency response of the piezoelectric-based sensor there is a large difference in the measured impulse (gray area), however the peak pressures are similar especially when measured as a fit to a decaying exponential (gray lines).

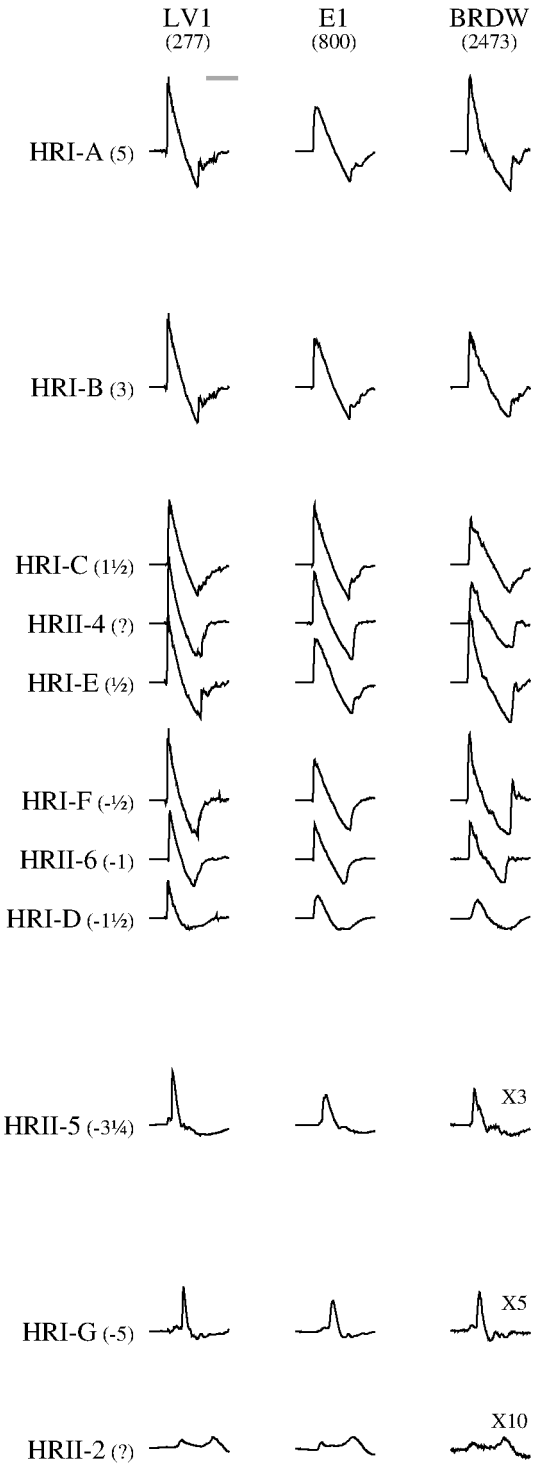

Figure 12. Pressure waveforms for selected stations that recorded multiple events (no data for HRII-1 and null observation at HRII-3) organized by scaled hob and scaled distance and the amplitude is scaled by distance. Distance [m] and hob [m] for each station or shot are given in parenthesis. The lower three traces are multiplied by an additional factor for visibility.

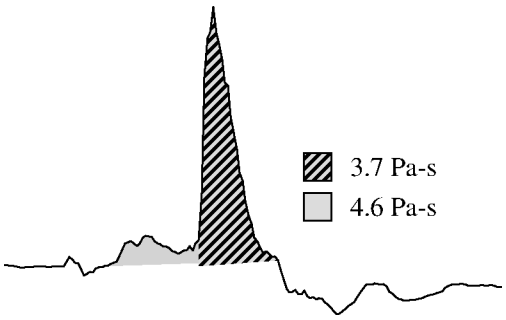

Figure 13. HRI-G (hob=–5m) recorded at LV1 (range=275m). The positive phase area (impulse) measured beginning at the most impulsive arrival (hachured pattern) is 80% of the total positive phase area (gray). The trace is 0.17 s long.

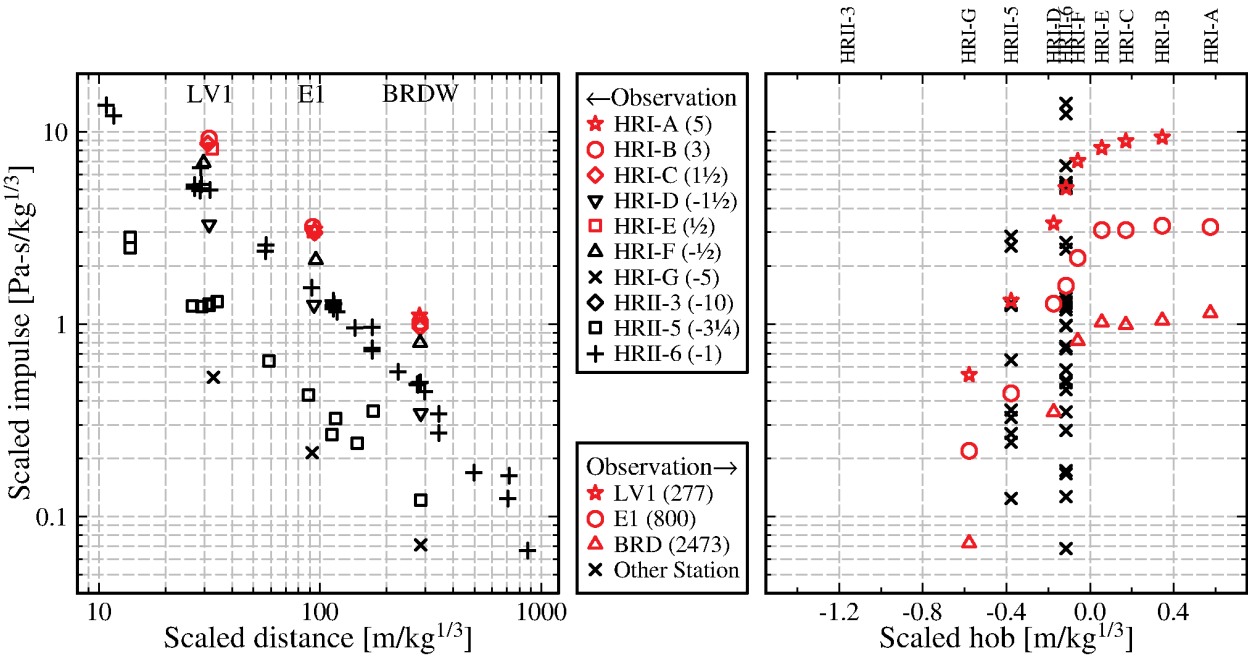

Figure 14. Scaled impulse versus scaled distance (left) and hob (right). The symbols represent the shots in the left panel (red are above-ground and black are below-ground), and select stations in the right panel (red), since labeling all stations would clutter the figure. Only diaphragm-based measurements (Validyne) are used for HRI shots (see text for details). The select stations are labeled at their approximate distance at the top of the left panel and the shots are labeled at their hob at the top of the right panel.

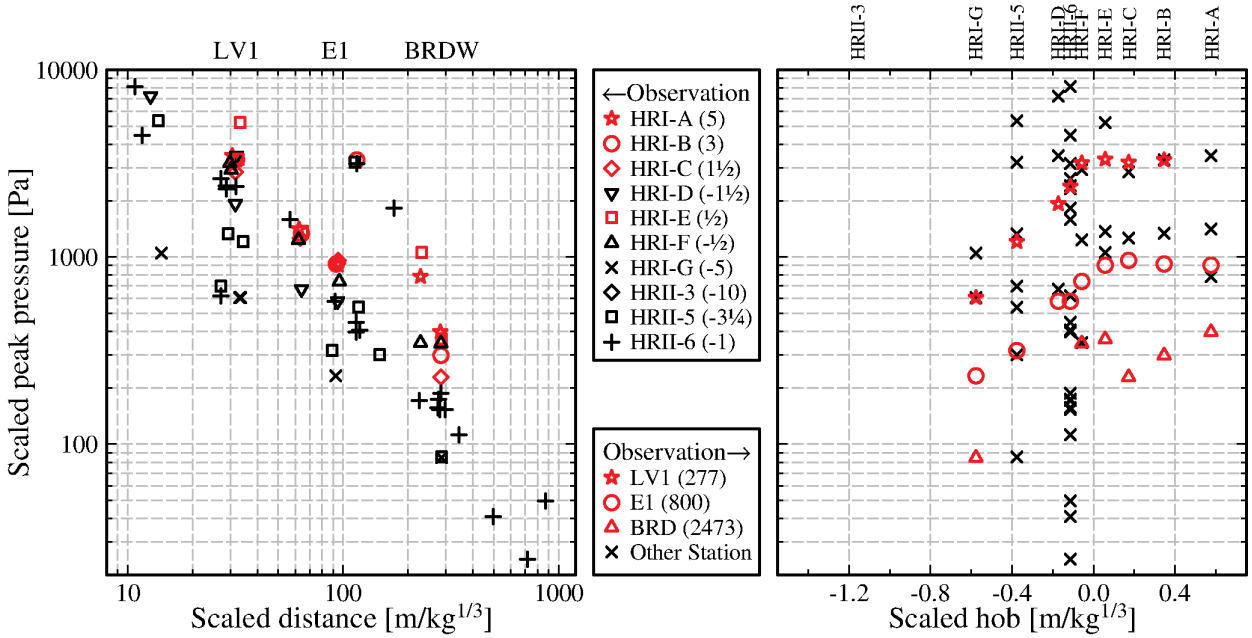

Figure 15. Scaled pressure versus scaled distance (left) and hob (right). The symbols represent the shots in the left panel (red are above-ground and black are below-ground), and select stations in the right panel (red), since labeling all stations would clutter the figure. The select stations are labeled at their approximate distance at the top of the left panel and the shots are labeled at their hob at the top of the right panel.

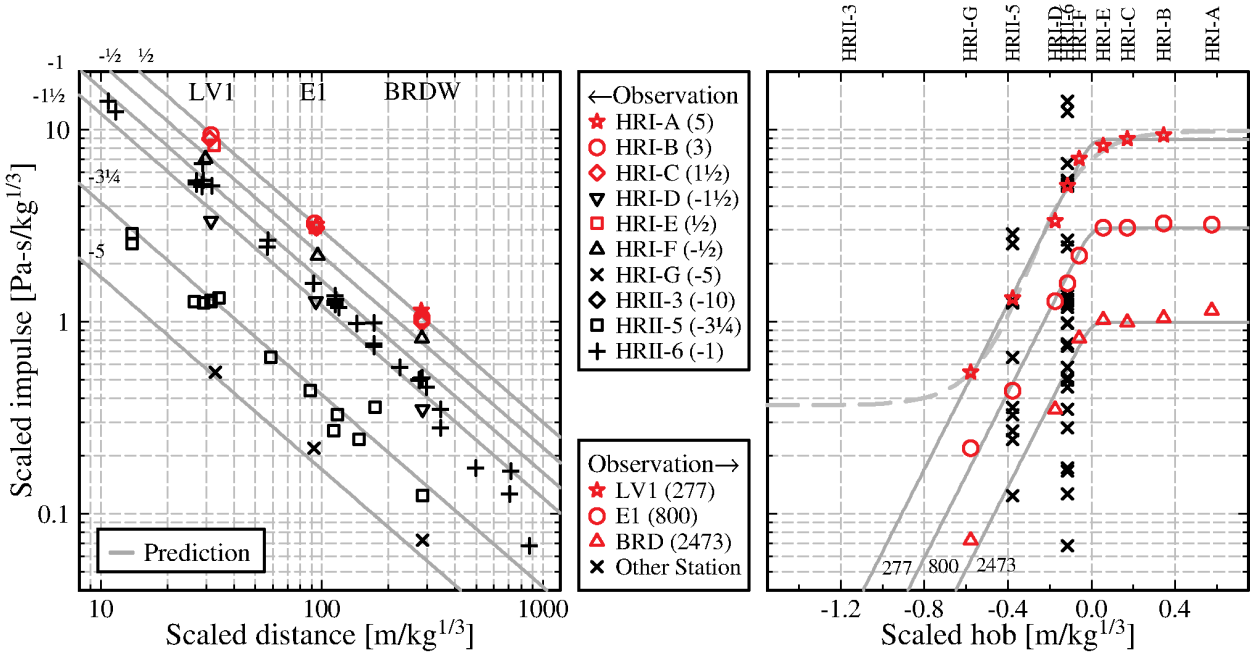

Figure 16. Same as Figure 14 but with predictions (gray lines) based on equation (3) with parameters in Table 2. The hobs in meters used to make the predictions in the left panel are given at the top-left. The distances in meters (average to each station) used to make the predictions in the right panel are given at the bottom of each line. An alternative model, discussed in the text, is given by the dashed line.

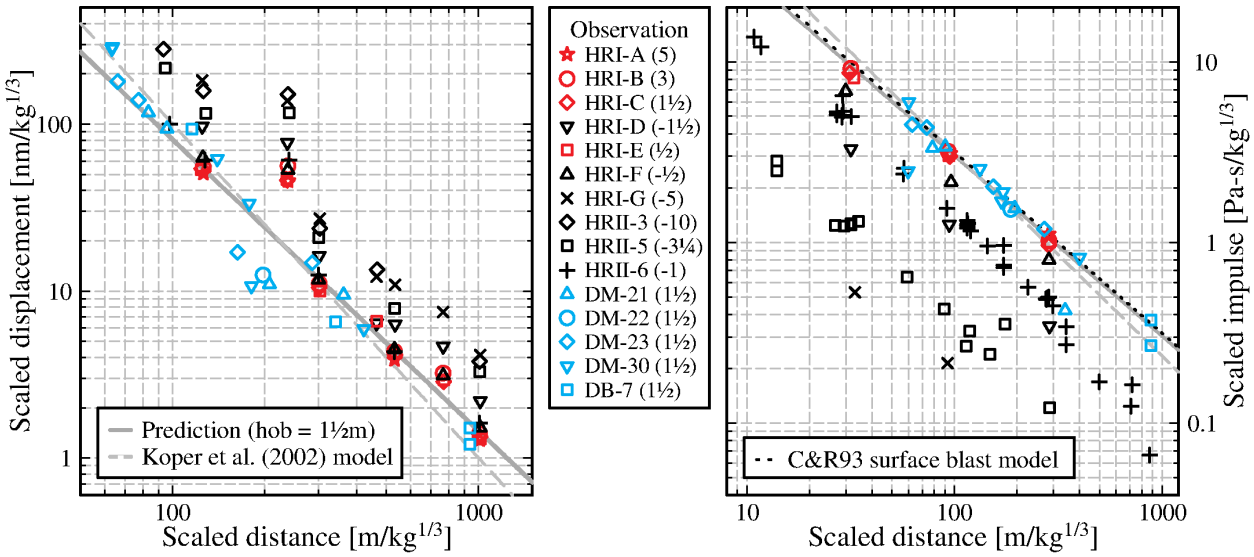

Figure 17. Dipole-Might and Divine-Buffalo test series observations. All shots were at ~1.5m. Observations at station MCDR (points at ~200 scaled-distance) has some unaccounted seismic site response.

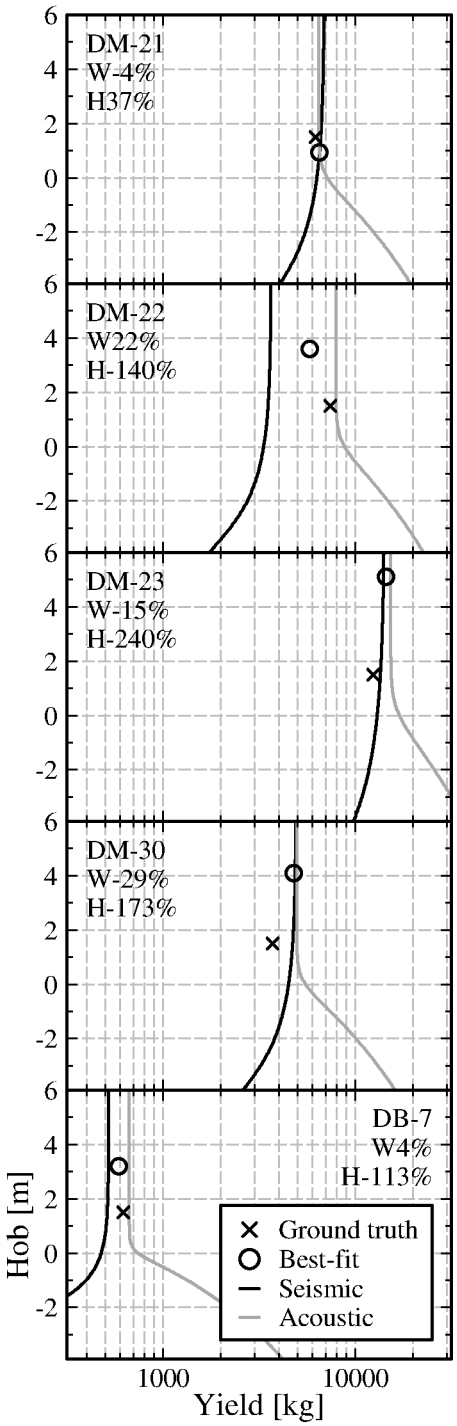

Figure 18. Seismic and acoustic curves trace out the best-fit solutions for each dataset. Best-fit solution (circle) is the lowest combined log residual. The percent error in yield (W) and height-of-burst (H) is given below each shot name. Notice that due to models there is little resolution at hob>2m.

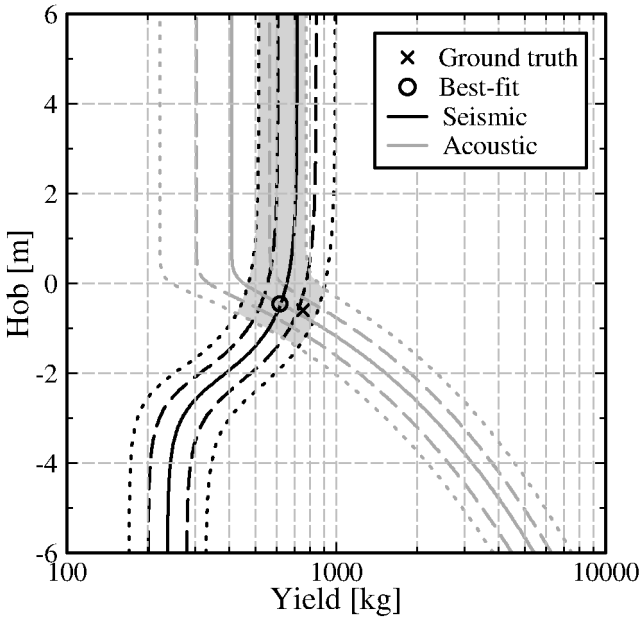

Figure 19. Prediction of HRII-4 yield and hob where the ground truth (754 kg @ -0.6m) is compared with the best-fit solution (620 kg @ –0.5 m, circle) is found via a grid-search of the coupled seismic (black line) and acoustic (gray line) models. Error in the models are used to contour 1- (dashed line) and 2-sigma (dotted line) confidence regions. The 2-sigma region (gray area) is bounded by 400 kg ≤ yield ≤ 900 kg and hob ≥ –1.5 m. The 1-sigma region is bounded by 500 kg ≤ yield ≤ 720 kg and –1 m ≤ hob ≤ 0.3 m.

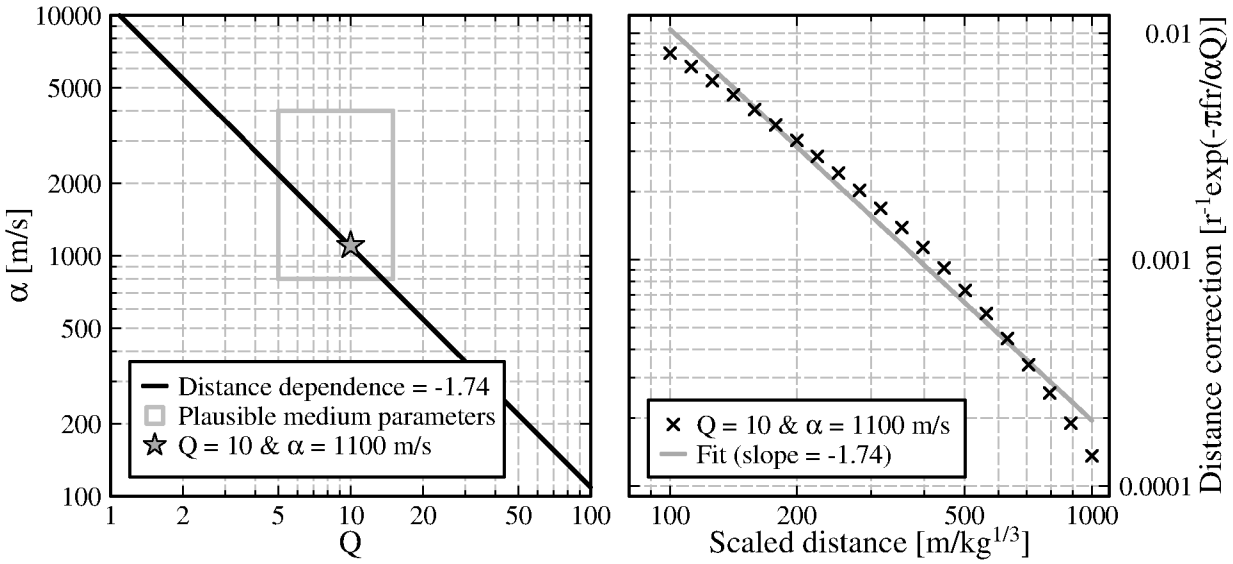

Figure 20. We fit the distance dependent term (β_2 = –1.74) from equation (1) to a loss function that incorporates spherical spreading and attenuation, where one set of medium parameters out of plausible choices (gray box) is Q=10 and a=1100 m/s (star). The distance correction is compared with the distance dependent term in the right panel, which is looks to be appropriate over the scaled distance range in this study.

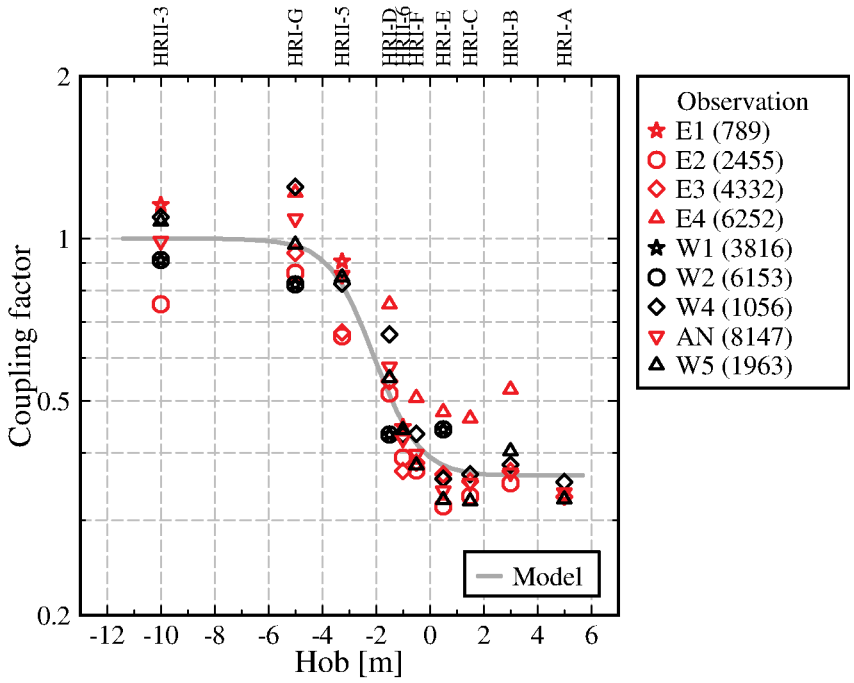

Figure 21. Seismic coupling curve. The distance dependence of the data is removed using the first two terms in equation (1) with a site correction for station W5. The corrected data is then plotted with a tanh curve using the coefficients given in Table 1 and shifted to obtain a coupling of 1 for deeply buried shots.

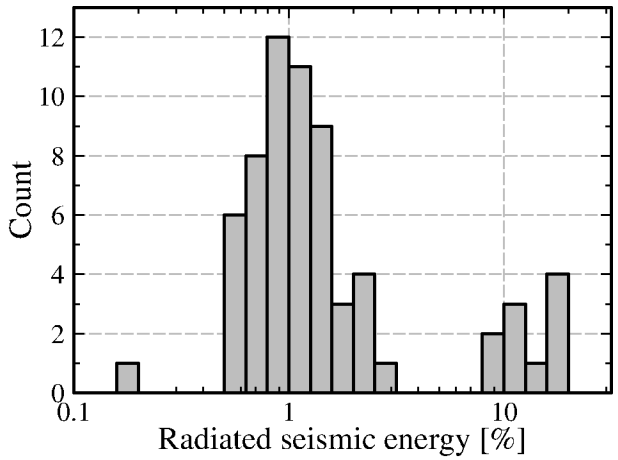

Figure 22. Distribution of estimated seismic efficiency (radiated seismic energy / explosive chemical energy) of the HR explosions. Without W5 (grouping near 10%), which looks to have an unaccounted site response, the average is 1% and range is ½-2%.